JGR Oceans

RESEARCH ARTICLE
10.1029/2019JC015259

Special Section:
Contributions from the Physics of Estuaries and Coastal Seas meeting, 2018

The Impact of Wind Forcing on the Thermal Wind Shear of A River Plume

P. L. F. Mazzini[1], R. J. Chant[2], M. E. Scully[3], J. Wilkin[2], E. J. Hunter[2], and N. J. Nidzieko[4]

[1]Estuary and Ocean Science Center, San Francisco State University, Tiburon, CA, USA, [2]DMCS, Rutgers, The State University of New Jersey, New Brunswick, NJ, USA, [3]Applied Ocean Physics and Engineering, Woods Hole Oceanographic Institution, Woods Hole, MA, USA, [4]Department of Geography, University of California, Santa Barbara, CA, USA

Abstract A 38-day long time series obtained using a combination of moored Wirewalkers equipped with conductivity-temperature-depth profilers and bottom-mounted and subsurface acoustic Doppler current profilers provided detailed high-resolution observations that resolved near-surface velocity and vertical and cross-shelf density gradients of the Chesapeake Bay plume far field. This unprecedented data set allowed for a detailed investigation of the impact of wind forcing on the thermal wind shear of a river plume. Our results showed that thermal wind balance was a valid approximation for the cross-shelf momentum balance over the entire water column during weak winds ($|\tau_y^w| < 0.075$ Pa), and it was also valid within the interior during moderate downwelling ($-0.125 < \tau_y^w < -0.075$ Pa). Stronger wind conditions, however, resulted in the breakdown of the thermal wind balance in the Chesapeake Bay plume, with thermal wind shear overestimating the observed shear during downwelling and underestimating during upwelling conditions. A momentum budget analysis suggests that viscous stresses from wind-generated turbulence are mainly responsible for the generation of ageostrophic shear.

Plain Language Summary Historically, oceanographers have been using a theoretical framework that allows us to estimate current velocities from water density profiles, commonly obtained during oceanographic cruises. This technique has been used to calculate transport of water and heat carried by the Gulf Stream toward the poles and to study other major currents in the deep ocean. The same theoretical framework has also been applied to study currents in shallow coastal regions (10-20-m), however, without a thorough validation. In this work, we test and validate this theoretical framework in the Chesapeake Bay Plume, which is brackish water originated from the Chesapeake Bay off the coasts of Virginia and North Carolina. We use novel high-resolution measurements obtained by a series of moored instruments that include current meters and two Wirewalkers, which are wave-powered profiling platforms that were equipped with salinity and temperature sensors and that allowed us to obtain a rich data set with thousands of density profiles. We found that theory and observations agree when winds are weak or moderate. However, during strong winds, we found that the theory breaks down due to wind-generated turbulence (irregular motion resulting from eddies), and a correction for using this theory in shallow areas is necessary.

Key Points:
- Novel data set allowed evaluation of thermal wind shear in river plumes in response to wind forcing
- During weak winds, thermal wind balance is a valid approximation in a river plume but breaks down during strong winds
- Thermal wind shear overestimates (underestimates) observed shear during downwelling (upwelling)

Correspondence to:
P. L. F. Mazzini,
pmazzini@sfsu.edu

Citation:
Mazzini, P. L. F., Chant, R. J., Scully, M. E., Wilkin, J., Hunter, E. J., & Nidzieko, N. J. (2019). The impact of wind forcing on the thermal wind shear of a river plume. *Journal of Geophysical Research: Oceans*, *124*, 7908–7925. https://doi.org/10.1029/2019JC015259

Received 2 MAY 2019
Accepted 18 OCT 2019
Accepted article online 29 OCT 2019
Published online 17 NOV 2019

The copyright line for this article was changed on 4 FEB 2020 after original online publication.

1. Introduction

River plumes are oceanographic features ubiquitous to continental shelves worldwide, responsible for the transport and dispersion of micronutrients and macronutrients, larvae, sediments, and pollutants originating from rivers and estuaries (Hill, 1998). Thus, they play a crucial role in the marine biogeochemistry (Sharples et al., 2017), continental shelf sediment budget (Geyer et al., 2004), and shaping coastal ecosystems (Hickey et al., 2010). To properly diagnose the mechanisms controlling plume transport, mixing and dispersion, it is crucial to understand the dominant terms of the momentum budget. Away from an estuary's mouth, (i.e., far field), it is widely accepted by the scientific community that the first-order momentum balance in the plume's cross-shelf direction is between the pressure gradient force and the Coriolis acceleration (i.e., Chant, 2011; Chapman & Lentz, 1994; Garvine, 1995; Horner-Devine et al., 2015; Lentz & Helfrich, 2002; Yankovsky & Chapman, 1997); that is, along-shelf currents are in geostrophic balance.

A number of studies interpreting in situ observations, numerical model results, or developing analytical theories and scalings rely on the assumption of geostrophy in far-field river plumes (Avicola & Huq, 2003; Fong & Geyer, 2002; Lentz & Helfrich, 2002; Mazzini & Chant, 2016; Mazzini et al., 2014; Moffat & Lentz, 2012; Pimenta et al., 2011; Yankovsky & Chapman, 1997). Since the majority of small- to medium-sized plumes are restricted to shallow environments (O(1–10) m), where the turbulent surface and bottom boundary layers are expected to encompass a significant fraction of the water column (Austin & Lentz, 2002), the geostrophic assumption may not hold, and validation is needed. Nevertheless, attempts to verify the cross-shelf geostrophic balance in river plumes are scarce and based on limited data in either space and/or time (O'Donnell, 2010).

1.1. Background

As it is difficult to estimate absolute geostrophic currents due to uncertainty in the "level of no motion," previous authors have estimated the vertical shear of geostrophic currents, taking advantage of the thermal wind balance, which can be written as

$$\frac{\partial v_g}{\partial z} = -\frac{g}{\rho_0 f}\frac{\partial \rho}{\partial x}, \tag{1}$$

where v_g is the geostrophic current, g is the gravitational acceleration, ρ_0 is a reference density, f is the Coriolis parameter, ρ is density, and z and x are the vertical and cross-shelf coordinates, respectively. $\partial v_g/\partial z$ will be referred to here as the thermal wind shear (TWS), and from equation (1) it can be calculated directly from measurements of horizontal density gradients ($\partial\rho/\partial x$), without a priori knowledge of a "level of no motion." Evaluation of the geostrophic balance in a plume can be done by directly comparing TWS estimated using equation (1), to the observed vertical shear of along-shelf currents (OBS) derived from measurements of velocity profiles.

To the best of our knowledge, the first attempt to investigate the geostrophic balance in a river plume was conducted by Blanton (1981). The author analyzed data collected during 50 hr using two anchored ships, which collected simultaneous hourly profiles of density and currents across a frontal zone off the coast of Georgia, in water depths between 14 and 16 m during light downwelling-favorable winds. Qualitative assessment of the geostrophic balance was provided as can be seen in Figure 10 by Blanton (1981); however, TWS clearly overestimated the OBS during this campaign.

A more detailed analysis was provided by Garvine (2004), during a study of the Hudson River plume, New Jersey. Using data from acoustic Doppler current profilers (ADCPs) moored between 12 and 25 m, combined with density profiles obtained during cruises using a conductivity, temperature, and depth (CTD) profiler and a towed undulating vehicle (Scanfish) with a CTD, the author demonstrated similarities between TWS and OBS (equation (1)). By selecting 15 profiles, Garvine (2004) showed that depth averaged values of OBS were significantly correlated with their TWS counterparts (correlation coefficient $r = 0.69$).

Yankovsky (2006) conducted perhaps the most in-depth study of the topic up to date. Using data from the same field campaign as in Garvine (2004), Yankovsky (2006) combined the shipboard ADCP data with the density measurements from the Scanfish, to estimate the spatial distribution of the TWS. The data set was limited to only seven transects obtained during 4 days under weak wind conditions. The author found that on average TWS overestimated OBS by a factor of 2 and hypothesized that the decrease in the OBS could be due to turbulent production generated by internal wave breaking.

It is important to emphasize that the conclusions obtained from previous findings cited above are based on data sets that lack information in the first few meters near the surface and are only representative of weak wind-forcing conditions. With these restrictions in mind, the common findings from previous work may be summarized in two main points: (1) OBS are qualitatively similar and correlated to TWS and (2) OBS magnitudes are generally smaller (nearly half) of those predicted by TWS. It is still unclear whether these conclusions maybe extrapolated to the near-surface and how they may be impacted by different wind-forcing regimes.

1.2. Study Goals

In the present paper, we evaluate the cross-shelf geostrophic balance (TWS) in the far field region of the Chesapeake Bay Plume (CBP) (Figure 1), using high-resolution data collected by two cross-shelf moorings equipped with bottom mounted and subsurface ADCPs, as well as CTD profiles obtained with Wirewalkers (WW) (Pinkel et al., 2011; Rainville & Pinkel, 2001). With 39,200 CTD profiles recorded over 38 days (23 April

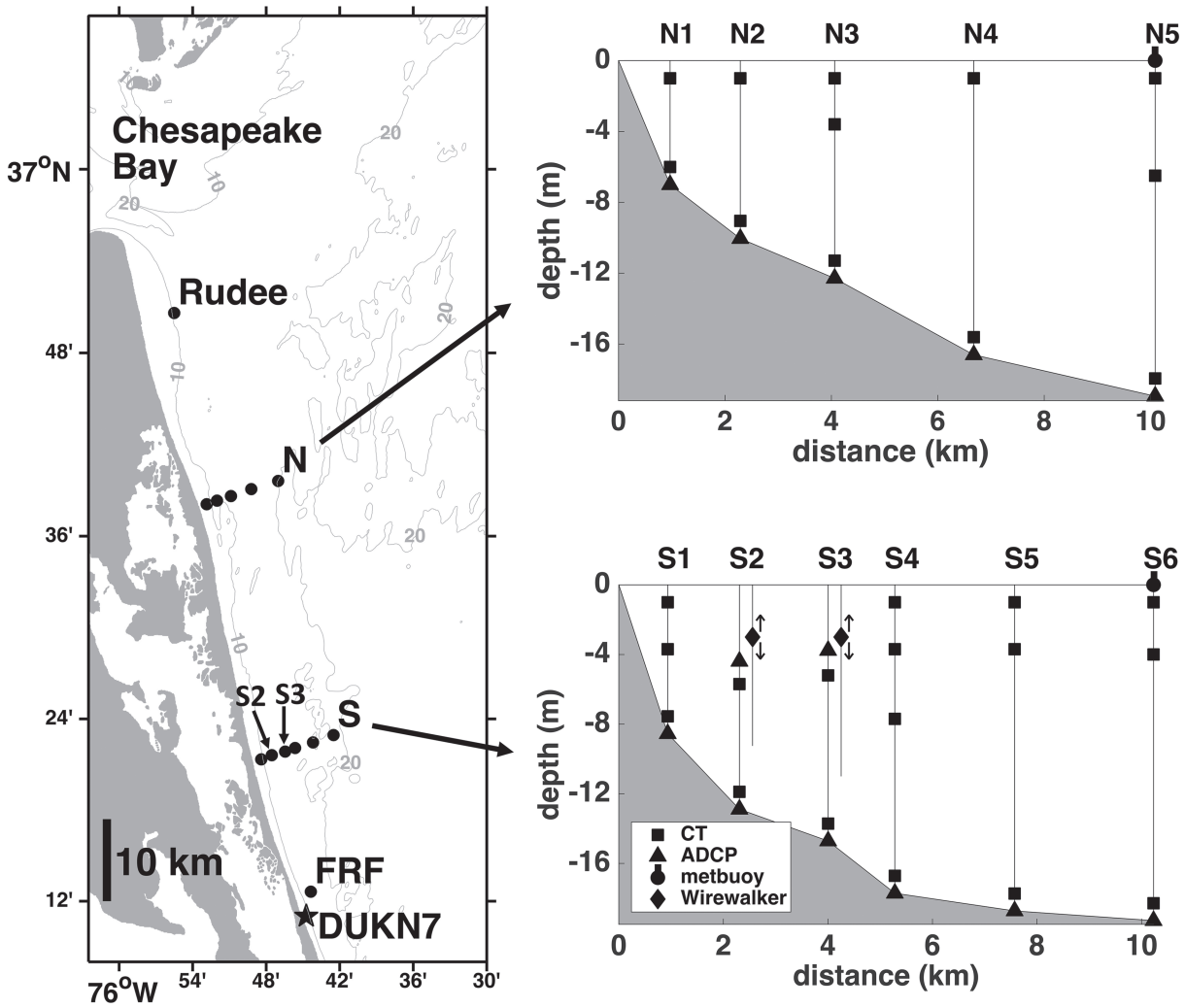

Figure 1. (left) Map of study area including mooring locations (filled circles) and meteorological station DUKN7 (star). (right) Vertical distributions of moored instruments on N and S lines. Details on mooring instrumentation are listed in Table 1.

2015 to 31 May 2015) under a wide range of wind conditions, this data set allows the careful examination of the near-surface TWS and the effect of wind forcing on this basic balance. Our goals are thus to (1) quantify the validity of thermal wind balance in the far-field plume in a range of along-shelf wind-forcing regimes, (2) identify the dynamical terms that are responsible for generation of agesotrophic shear, and (3) address the impact of wind forcing on plume transport.

2. Data and Methods

2.1. Observations

Data used in this paper were collected during the project "Circulation and Mixing in a Coastally Trapped River Plume," funded by the National Science Foundation. Thirteen moorings equipped with conductivity-temperature (CT) sensors and ADCPs were deployed off the coasts of Virginia and North Carolina (Figure 1) during the Spring season (May–June) of 2015. Here, we analyze data from the moorings N2 and N3 from the N line, and S2 and S3 from S line, located 35 and 64 km south of the Chesapeake Bay mouth, respectively. Details of the mooring instrumentation are shown in table 1. The major focus of this paper relies on the unprecedented data obtained by moorings S2 and S3, which were equipped with bottom and subsurface CTs and ADCPs, and WWs, providing high-temporal and spatial resolution of cross-shelf density gradients and currents, including the near surface region (0.5–1 m from surface).

Table 1
Summary of Instrumentation on Moorings N2, N3, S2, and S3 (Figure 1)

Mooring	Water depth (m)	Offshore distance (km)	Location	Instrument type	Instrument depth (m)	Sampling frequency (Hz)	Vertical Resolution (m)
N2	10.1	2.3	36°38.3′N, 75°52.0′W	CT	1, 9.6	2	
				ADCP	9.6	1	0.5
N3	12.3	4.1	36°38.6′N, 75°50.9′W	CT	1, 3.6, 11.8	2	
				ADCP	11.8	1	0.5
S2	12.9	2.3	36°21.6′N, 75°47.5′W	CT	5.7, 12.4	2	
				ADCP	5.7, 12.4	1, 4	0.25, 0.5
				Wirewalker	0.5–9.2	2	
S3	14.7	4.0	36°21.9′N, 75°46.5′W	CT	5.2, 12.2	2	
				ADCP	5.2, 12.2	1, 1	0.25, 0.5
				Wirewalker	0.5–11.0	2	

WWs are vertically profiling platforms propelled by ocean waves, that can carry instruments on board, collecting extensive time series of ocean properties with high vertical and temporal resolution (Pinkel et al., 2011; Rainville & Pinkel, 2001). Time series of temperature and salinity were collected by the WWs between 23 April 2015 and 31 May 2015, a total of 38 days. During this time, over 21,150 and 18,050 profiles were collected at moorings S2 and S3, respectively. The profiles were obtained between 0.5 and 9.2 m deep for S2 and between 0.5 and 11 m for S3, with median profiling times of 1.4 and 1.8 min for S2 and S3, respectively. WW data were combined into 0.25 m bins in the vertical and binned in 10 min intervals. Density was then calculated from temperature and salinity using the 1980 equation of state (EOS-80).

The ADCPs used in this study had working frequencies of 1,200 kHz and were programed to sample at 1 Hz, with the exception of the bottom-mounted ADCP at S3, which had working frequency of 1,000 kHz and 4 Hz sampling frequency. Subsurface ADCPs were programed to provide vertical resolution of 0.25 m, while the ones deployed at the bottom had 0.5 m vertical resolution (Table 1). Current data were binned in 10 min intervals, consistent with density measurements, and rotated into the along- and across-shelf direction (104.6° and 14.6° measured counterclockwise from the east, respectively).

Wind velocity and direction were obtained from the pier at Duck, NC, Station DUKN7-8651370 (36°11.0′N, 75°44.8′W), maintained by the National Oceanic and Atmosphere Administration's National Ocean Service. Wind stress was computed based on the Large and Pond (1981) formulation, binned in 10 min intervals, and decomposed into along- and across-shelf directions, consistent with current data. To isolate low-frequency components, the time series of salinity, temperature, velocity and wind stress, were low-pass filtered with a cut-off period of 40 hr.

2.2. OBS, TWS, and Ageostrophic Along-Shelf Vertical Shears

To estimate the vertical shear of observed along-shelf currents (OBS), $\partial v_{obs}/\partial z$, low-passed velocity data from bottom-mounted and subsurface ADCPs were spatially averaged between moorings S2 and S3. Vertical shears were then estimated using centered differences for the spatially averaged velocities, separately for bottom-mounted and subsurface velocity data. Finally, the estimated shears and velocities were interpolated to the same vertical coordinates as in the WW data, with 0.25 m resolution.

The TWS, $\partial v_g/\partial z$ (equation (1)), was calculated by applying centered differences to the low-passed density data from the WWs at S2 and S3, located 1.7 km apart, and using a reference density ρ_0 of 1,025 kg/m^3, gravitational acceleration g of 9.81 m/s^2, and the Coriolis parameter $f = 8.65\times10^{-5}$ s^{-1} (36°21.7′N). Following Yankovsky (2006), we will define the ageostrophic shear (AGEOS) $\partial v_a/\partial z$, as simply the difference between OBS and TWS:

$$\underbrace{\frac{\partial v_a}{\partial z}}_{\text{ageostrophic shear (AGEOS)}} = \underbrace{\frac{\partial v_{obs}}{\partial z}}_{\text{observed shear (OBS)}} - \underbrace{\frac{\partial v_g}{\partial z}}_{\text{thermal wind shear (TWS)}} . \quad (2)$$

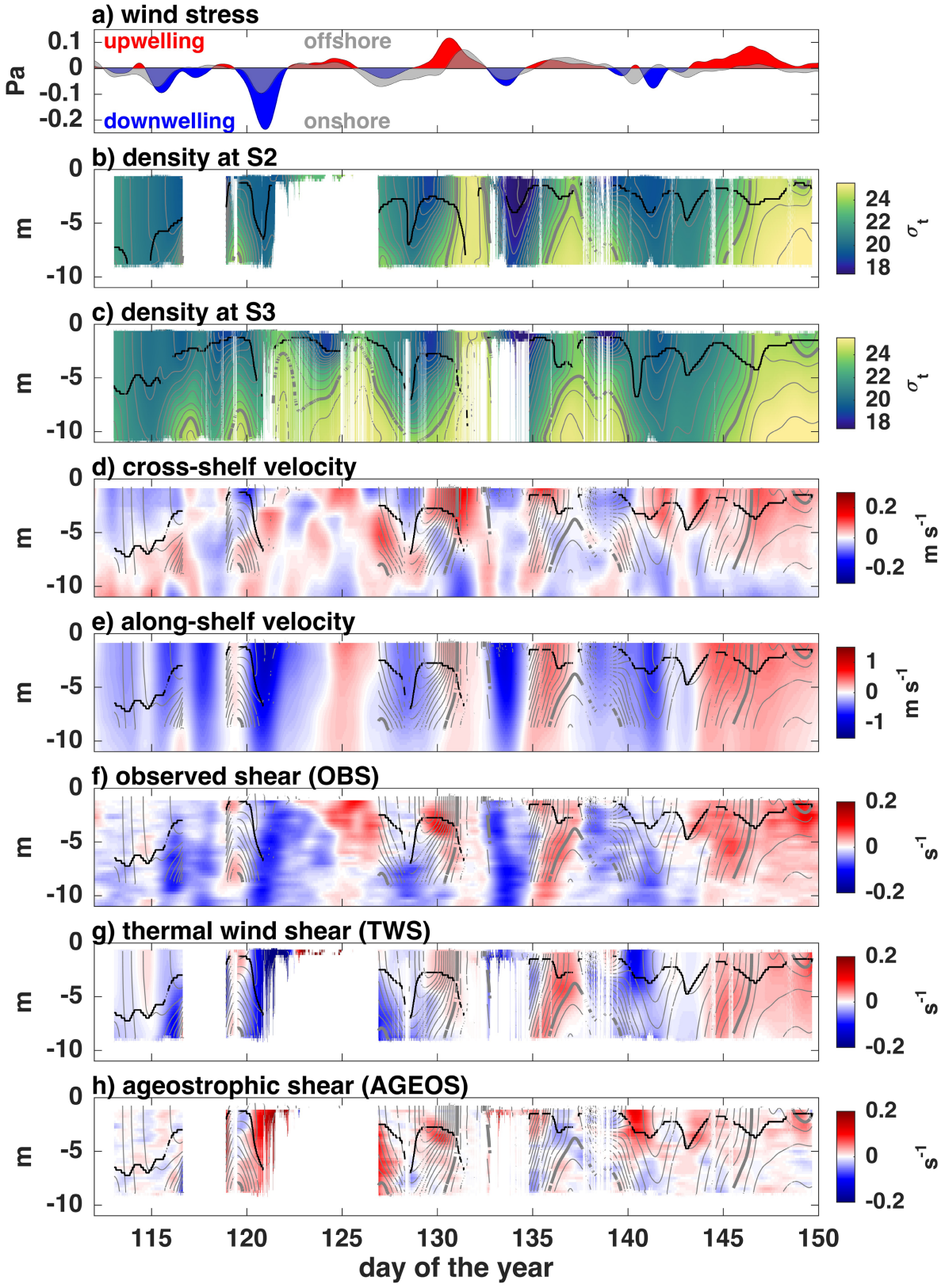

Figure 2. Time series of (a) wind stress; (b) S2 and (c) S3 densities (σ_t); (d) cross- and (e) along-shelf velocities averaged between S2 and S3; and (f) observed (OBS), (g) thermal wind (TWS), and (h) ageostrophic (AGEOS) along-shelf vertical shears. Density is contoured in intervals of 0.5 σ_t, thick gray line denotes 24 σ_t which is an approximate limit for the CBP, and surface mixed layer depth is plotted in black. Panels d–h are overlayed with contours of average density between S2 and S3 and mixed layer depth of the averaged density field.

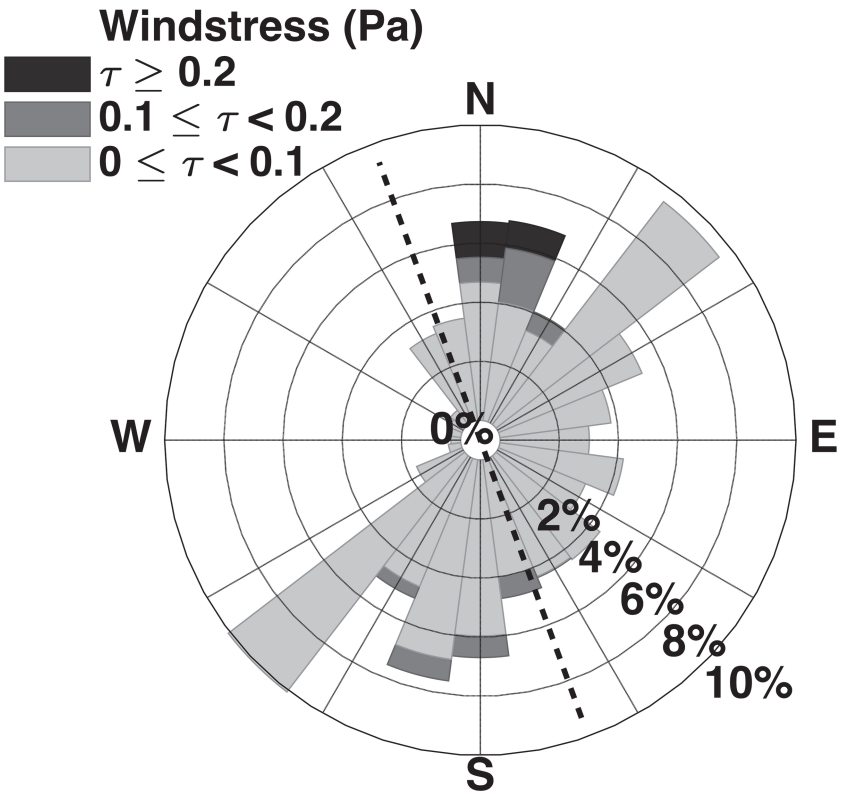

Figure 3. Directional histogram of low-passed wind stress during the study period. Bars point toward the direction where the winds are coming from (meteorological convention), and dashed line indicates the coastline orientation.

3. Results

3.1. Wind Stress Forcing

A time series of low-passed wind stress at station DUKN7 (Figure 1) during the study period (23 April to 31 May 2015) is shown in Figure 2a, with along-shelf positive representing upwelling- and negative representing downwelling-favorable winds, and cross-shelf positive representing winds blowing toward offshore and cross-shelf negative representing winds blowing toward onshore. Results are summarized by the directional histogram in Figure 3.

Most of the wind stress energy is contained in the weather band (2–7 days) associated with the passage of frontal systems, with higher-frequency oscillations (not shown) accounting for less than 35% of the total variance. Cross- and along-shelf components have small means, −0.01 and −0.002 Pa, with standard deviations over 3 and 22 times larger than the means, respectively. In contrast to the west coast, winds are not predominantly oriented along the shelf (e.g., Halliwell et al., 1987), with the direction of maximum variance departing 30° clockwise from the coastline orientation during the study period. This results in substantial cross-shelf wind stress components, which are correlated with the along-shelf winds (Figures 2 and 3). While the time series represent a range of wind conditions that will be explored in our analysis, including seven upwelling/downwelling events and magnitudes reaching over 0.25 Pa, the data record is not long enough to systematically separate along- and cross-shelf wind stress forcings (e.g., Fewings et al., 2008), and therefore it is important to note that downwelling-/upwelling-favorable winds are correlated with onshore/offshore winds.

3.2. WW Observations

High-resolution time series of density obtained by the WWs at S2 and S3 are shown in Figures 2b and 2c. The WW data has gaps due to wire tilt in swift currents (1 m/s) that prevented the profiler from ratcheting downward into the oncoming flow. Gaps are also present at random times due to low waves or instrument failure. Nevertheless, over 39,200 CTD profiles were obtained, which in combination with velocity data from moored ADCPs, allowed the calculation of OBS, TWS and AGEOS (equations (1) and (2)) (Figures 2f–2h).

The 24 σ_t contour (thick gray line in Figure 2), which corresponds to salinity values between 32 and 32.5, is an approximate indicator of the CBP edge. Below the plume, stratification is weaker but persistent, maintained by contributions of both salinity and temperature gradients (not shown). The CBP is present at both the S2 and S3 moorings during over 87.5% of the survey period, with salinities ranging between 24.6 and 33.7, and temperatures between 9.6 and 20.8 °C (not shown). While waters associated with the CBP are generally warmer than adjacent shelf waters, nearly 80% of density variations are controlled by salinity variability, with temperature playing a secondary role. Density gradients between S2 and S3 are on average 0.08 (±0.4) kg/m^3 km^{-1}, with maximum value of 2.6 kg·m^{-3}· km^{-1}. These correspond to an average TWS of 0.01 (±0.04) s^{-1} and a maximum of 0.3 s^{-1}.

CBP is a surface advected river plume, and therefore is highly responsive to wind forcing (Lentz & Largier, 2006). Approximately 13 wind reversals occurred during this period, allowing characterization of the vertical shears under both upwelling and downwelling condititions, and a wide range of wind stress magnitudes (Figures 2 and 3). As shown in Figure 2, the pycnocline gets deeper and density decreases in the presence of downwelling-favorable winds, while during upwelling-favorable winds the pycnocline gets shallower and density increases.

This can be explained in terms of Ekman dynamics: downwelling-favorable winds result in an onshore surface Ekman transport and offshore transport in the bottom, which leads to steepening of the isopycnals, consequently increasing the TWS and therefore the along-shelf freshwater transport (Moffat & Lentz, 2012); upwelling-favorable winds generate offshore surface Ekman transport and onshore transport in the bottom, which advects the plume offshore flattening the isopycnals, decreasing the along-shelf transport (Fong & Geyer, 2001; Lentz, 2004). During times of strong or sustained upwelling-favorable winds, offshore Ekman transport can detach the CBP from the coast (Lentz & Largier, 2006; Pimenta & Kirwan, 2014), which can be observed during Days 131–132 and 146–148, denoted by the disappearance of σ_t values lower than 24.

3.3. Cross- and Along-Shelf Velocities

During many instances the cross-shelf velocity data (Figure 2d) support this simple two-dimensional, two-layer cross-shelf circulation with offshore flow in the surface and onshore flow beneath in response to upwelling-favorable winds, and onshore flow in the surface and offshore flow beneath in response to downwelling-favorable winds. Examples of these can be clearly seen during Days 129–132 and 143–150 for upwelling and Days 113–115, 120–121, and 141–142 for downwelling conditions. However, a more much complex cross-shelf circulation structure often is observed, including velocity with three layers (e.g., Days 116–117, 123–124, and 128–130), or onshore/offshore velocities occupying the entire profile (e.g., Days 133 and 134–135). This suggests that three-dimensional processes could play an important role in the plume dynamics (Hetland, 2017; Jia & Yankovsky, 2012), or the cross-shelf wind stress forcing could be significant (Jurisa & Chant, 2013) and therefore introducing more complexity to the cross-shelf flow. Nevertheless, the data does not allow us to disentangle these processes, which are beyond the scope of this paper. It will be demonstrated however, that this complex time variability in cross-shelf circulation fades away when averaging data into wind stress classes, and the classical two-dimensional cross-shelf Ekman driven circulation becomes evident (Figure 5c).

Time series of along-shelf velocity is shown in Figure 2e. Northward (positive) and southward (negative) velocities follow upwelling- and downwelling-favorable winds, however southward currents tend to be faster, reaching magnitudes as high as 1.2 m/s, contrasting maximum northward currents of 0.5 m/s. Winds may force currents in either direction, but the plume buoyancy-forcing (via TWS) drives southward velocities, and therefore the combined wind and buoyancy-forcing (e.g., Lentz & Largier, 2006; Mazzini et al., 2014) can explain the observed asymmetry in velocity magnitudes. Velocities increase in magnitude toward the surface, and also tend to have the same sign throughout the water column (top 10 m measured by the WWs). This indicates that the level of no motion of geostrophic currents remains deeper than the WWs water column coverage during this period or there is a significant barotropic velocity component.

3.4. Along-Shelf Vertical Shear

Time series of OBS, TWS and AGEOS are shown in Figures 2f–2h. OBS and TWS tend to have the same sign, with negative shear representing an increase in southward velocity toward the surface, and positive shear an increase in northward velocity toward the surface. They also consistently present the same signs as the velocities, and usually have constant sign throughout the water column. Following equation (2), AGEOS is defined here as the residual between OBS and TWS and is shown in Figure 2g. During downwelling events,

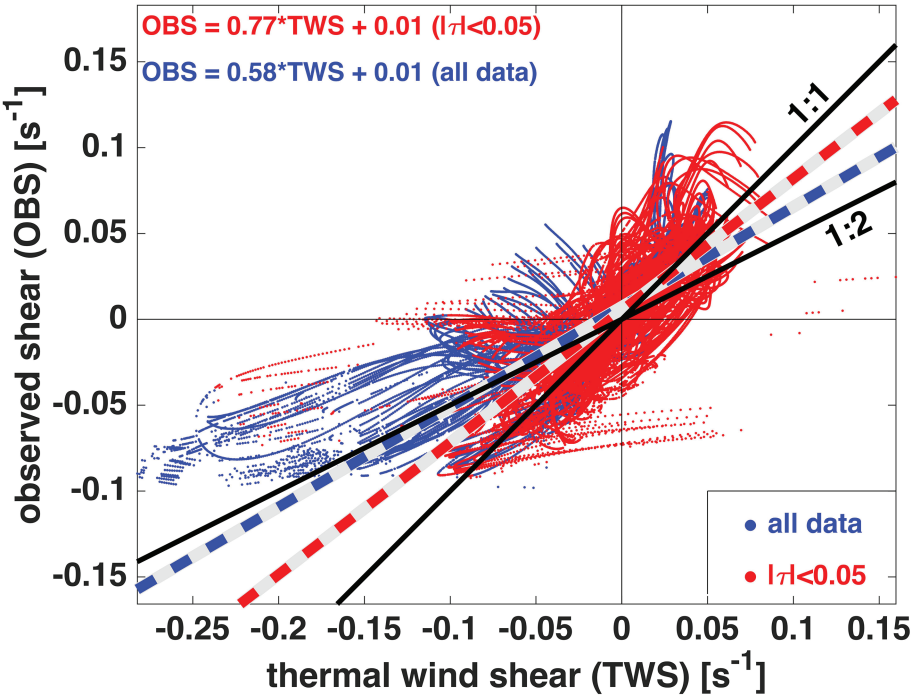

Figure 4. Thermal wind shear (TWS) versus observed shear (OBS). Full data set is plotted in blue dots, while data obtained during weak winds, defined here as $|\tau| < 0.05$ Pa, are plotted in red dots. Linear regressions fits are plotted as dashed lines for full data set (blue) and weak winds (red). Equations with slopes and intercepts values obtained from regression are included on top left. Slope 1:1 and 1:2 are plotted as solid black lines for reference.

TWS is consistently larger than OBS, and AGEOS has the opposite sign to TWS on Days 120–123, 127–128, and 133–135 (at the surface) and 140–144. During upwelling, TWS can be either larger or smaller than OBS; therefore, AGEOS can have the opposite sign (Days 119–120 and 135–138) or the same sign (Days 129–131 and 144–150, especially upper 5–6 m) as TWS and OBS.

To facilitate a direct comparison, OBS is plotted against the TWS in Figure 4 (in blue). While they are significantly correlated (correlation coefficient $r = 0.75$), TWS covers a larger range of values, between −0.28 and 0.16 s^{-1}, and OBS between −0.1 and 0.12 s^{-1}, approximately half of the TWS range. Performing a linear regression analysis between observed and TWS: We obtain a slope 0.58 and an intercept 0.01, which indicates that on average, TWS overestimates OBS by approximately a factor of 1.7. This result is consistent with the factor of 2 presented by Yankovsky (2006) in the Hudson River plume off New Jersey. The effect of wind forcing will be discussed next.

3.5. Wind-Forcing Effect on Shear

A regression analysis between OBS and TWS when winds were weak ($|\tau| < 0.05$), reveals a much closer agreement, with TWS overestimating OBS by approximately a factor of 1.3 (Figure 4, in red). This clearly demonstrates that wind forcing plays an important role influencing the thermal wind balance. Motivated by the contrasting vertical distribution of shears, which are enhanced in the upper 3–5 m (Figure 2h), we objectively divided the water column into the surface mixed layer (SML) and the interior. The SML depth was estimated by finding the maximum depth in which density is within $\Delta\rho = 0.1$ kg/m^3 of the shallowest density observation. By varying $\Delta\rho$ by plus or minus 50% our results (ratios of TWS/OBS over the interior and SML, Figure 6) changed by less than 7% during strong winds ($|\tau| > 0.15$) and less than 14% during weak to moderate winds ($|\tau| < 0.15$). The conclusions of this paper are not significantly affected by the choice of $\Delta\rho$. Average SML depth was found at 3.3 (±1.6) m.

We could not use similar methods to estimate bottom mixed layer (BML) depth because of a clear drift in the conductivity data from the bottom sensors. However, the persistent maintenance of stratification near the bottom limit of our WW data suggests that the WW was above the influence of the bottom boundary layer during the majority of the time. Therefore, in our analysis we will separate the water column into two regions only: the SML and the interior.

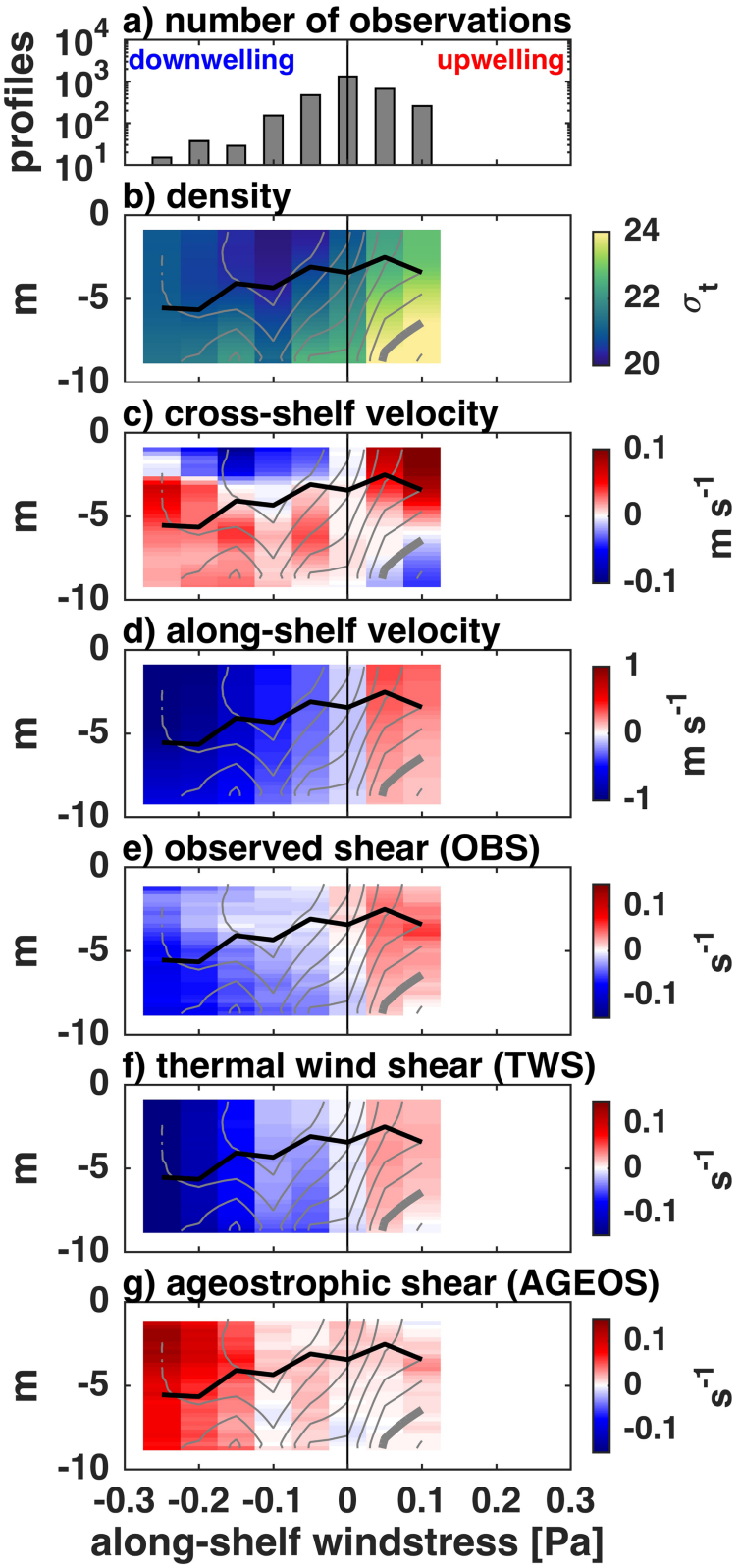

Figure 5. Binned data as a function of along-shelf wind stress classes. (a) Number of profiles used in the analysis; (b) density (σ_t); (c) cross- and (d) along-shelf velocities averaged between S2 and S3; and (e) observed (OBS), (f) thermal wind (TWS), and (g) ageostrophic (AGEOS) along-shelf vertical shears. Density is contoured in intervals of 0.5 σ_t, thick gray line denotes 24 σ_t which is an approximate limit for the CBP, and surface mixed layer depth is plotted in black, overlaying panels b–g.

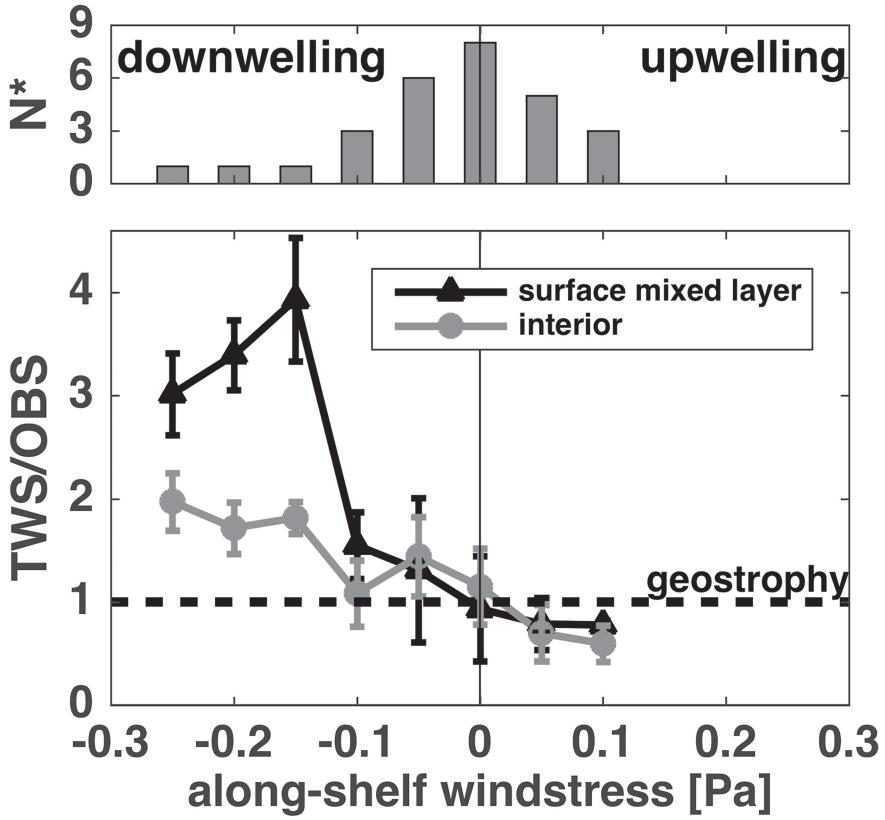

Figure 6. (top) Number of effective degrees of freedom (N*) for each wind stress class, used for calculating the standard error. N* is estimated assuming each crossing of a wind stress class corresponds to an independent observation. (bottom) Ratios between thermal wind (TWS) and observed (OBS) vertical shears binned as a function of wind stress. Calculations were done separately for the vertically averaged surface mixed layer (black) and interior (gray) regions. Errorbars represent one standard error from the mean, calculated using N*. Dashed line indicates exact geostrophic balance: TWS/OBS = 1.

To understand the impact of wind forcing on the CBP density structure, cross- and along-shelf circulation, and shears, all of the data were averaged as a function of wind stress classes. To avoid spatial biases, in this calculation we have only included full profiles, excluding times when WWs did not work properly and instead remained at the surface (e.g., between Days 123–124 and 132–135, Figure 2). Results are shown in Figure 5. The number of existing profiles for different wind stress classes is highly variable, ranging between 15 and over 10^3 profiles as shown in Figure 5a. It is important to emphasize however, that the number of independent observations or effective degrees of freedom (N*) is much smaller, as shown in Figure 6 (top panel). N* is estimated here assuming each crossing of a wind stress class corresponds to one independent observation. Note that only one independent observation is available for wind stress magnitudes greater than |0.1| Pa, and therefore the results and interpretations should be drawn in light of that.

An approximate linear decrease in density occurs from upwelling to downwelling until a mininum is observed centered at $\tau_y^w = -0.1$ Pa. Beyond that, density increases, likely due to enhanced mixing from wind-generated turbulence. As noted earlier, a simple cross-shelf circulation structure is revealed after binning the data, with offshore currents in the surface and onshore flow beneath during upwelling-favorable winds, and onshore currents in the surface and offshore flow beneath during downwelling-favorable winds. A decrease in near-surface onshore currents occurs during strong downwelling, however a complete reversal in cross-shelf circulation is not observed as reported by the models of Moffat and Lentz (2012) and Chen and Chen (2017). With a longer time series that includes stronger wind-forcing events it may be possible to test what is the wind stress magnitude required to reverse the cross-shelf circulation. The SML depth increases from 3.5 m in the absence of wind forcing to 5.5 m during strong downwelling. During weak downwelling ($|\tau_y^w|$ <0.15), SML depth coincides with the zero-crossing of cross-shelf velocities, but becomes deeper as winds increase. In contrast, SML depth always remains shallower than the zero crossing of cross-shelf

velocities during upwelling. Along-shelf velocity is positive during upwelling- and negative during weak and during downwelling-favorable winds. Velocity magnitudes increase as wind stress increases. Velocities are also enhanced in the upper half of the water column, generally above SML depth.

OBS is reduced near the surface (z >SML) and decreases as winds become negligible. During strong downwelling ($\tau_y^w < -0.15$ Pa) a maximum in shear is observed below the SML, while during strong upwelling (τ_y^w >0.1 Pa) the maximum is observed at the base of the SML, but reduced elsewhere. TWS exhibits smaller vertical variations when averaged as a function of wind stress. TWS is larger in magnitude than OBS during downwelling, but mostly smaller during upwelling. The resulting AGEOS is mostly positive during both upwelling and downwelling winds, except during very weak winds. AGEOS is enhanced during strong donwnwelling winds ($|\tau_y^w|$ >0.15 Pa), with a fourfold to sevenfold increase compared to weaker winds. A large contrast is also observed vertically, where strong downwelling winds increase AGEOS by a factor of 2 in the SML. In summary, AGEOS is mostly positive, increases significantly in the entire water column during strong downwelling-favorable winds ($|\tau_y^w|$ >0.15 Pa), but is especially enhanced in the SML.

3.6. SML Versus Interior

TWS and OBS were vertically averaged in the SML and interior, and the ratios TWS/OBS were calculated to evaluate thermal wind balance in these two distinct regions of the water column. To remove outliers, a 3-σ filter was applied 3 times to the ratio estimates, which resulted in the exclusion of less than 4% of data points from the interior and 7.5% of data points from the SML. To address the response to wind forcing, the ratios were again binned as a function of wind stress classes. Results from this calculation are shown in Figure 6 where the ratio TWB/OBS equal to one denotes exact geostrophic balance (dashed line in Figure 6). Errorbars denote one standard error above and below the mean, calculated using the number of wind events observed for each class as the true sample size (N*).

Within both the SML and interior regions, TWS is larger than OBS during downwelling- and smaller than OBS during upwelling-favorable winds. During weak winds ($|\tau_y^w| < 0.075$ Pa), ratios TWB/OBS are 1.3 during downwelling and 0.8 during upwelling in the SML, and 1.4 during downwelling and 0.7 during upwelling in the interior. Nevertheless in both cases TWB/OBS are within one standard error from a ratio equal to one. During moderate winds ($0.075< |\tau_y^w| < 0.125$ Pa), ratios are 1.5 during downwelling and 0.8 during upwelling in the SML, and 1.1 during downwelling and 0.6 during upwelling in the interior. Ratios are within one standard error from unity only in the interior during moderate downwelling conditions. Finally, for strong downwelling-favorable winds ($\tau_y^w < -0.125$ Pa), ratios TWB/OBS vary between 3 and 3.9 in the SML, and between 1.7 and 2 in the interior, and are statistically significant different than 1.

In summary, results show that the geostrophic assumption is valid over the entire water column during weak winds ($|\tau_y^w| < 0.075$ Pa), and it is also valid within the interior during moderate downwelling ($-0.125< \tau_y^w < -0.075$ Pa), but breaks down for stronger winds. During strong downwelling, TWS overestimates OBS by approximately a factor of 3–4 in the SML and a factor of 2 in the interior, while during upwelling the opposite is observed, TWS underestimates OBS with ratios 0.8 in the SML and 0.6 in the interior.

3.7. Cross-Shelf Momentum Balance

To assess the dynamics behind the breakdown of the thermal wind balance and generation of AGEOS, we will examine the vertical gradients of cross-shelf momentum budget (Ullman et al., 2012; Yankovsky, 2006). Taking the vertical derivative of the cross-shelf momentum balance, combined with the hydrostatic equation, and separating the along-shelf velocity into geostrophic and ageostrophic components $v = v_g + v_a$, results in

$$\frac{\partial}{\partial z}\left(\frac{\partial u}{\partial t} + u\frac{\partial u}{\partial x} + v\frac{\partial u}{\partial y} + w\frac{\partial u}{\partial z}\right) - f\left(\frac{\partial v_a}{\partial z} + \frac{\partial v_g}{\partial z}\right) = \frac{g}{\rho_0}\frac{\partial \rho}{\partial x} + \frac{\partial}{\partial z}\left(\frac{1}{\rho_o}\frac{\partial \tau_x}{\partial z}\right), \tag{3}$$

where y is the along-shelf coordinate, u, and w are the cross-shelf and vertical velocity components, respectively, τ_x is the stress in the cross-shelf direction, and other variables have been previously defined. Note that we decided to keep the full velocity v in the along-shelf advection term, for simplicity. From equation (3), it can be noted that the combination of the last term on the left hand side with the first term on the right hand side composes the thermal wind balance (equation (1)). Further isolating the agesotrophic from the gesotrophic part of equation (3), leads to

$$\frac{\partial v_a}{\partial z} = \frac{1}{f}\frac{\partial}{\partial z}\left(\frac{\partial u}{\partial t} + u\frac{\partial u}{\partial x} + v\frac{\partial u}{\partial y} + w\frac{\partial u}{\partial z} - \frac{1}{\rho_o}\frac{\partial \tau_x}{\partial z}\right). \tag{4}$$

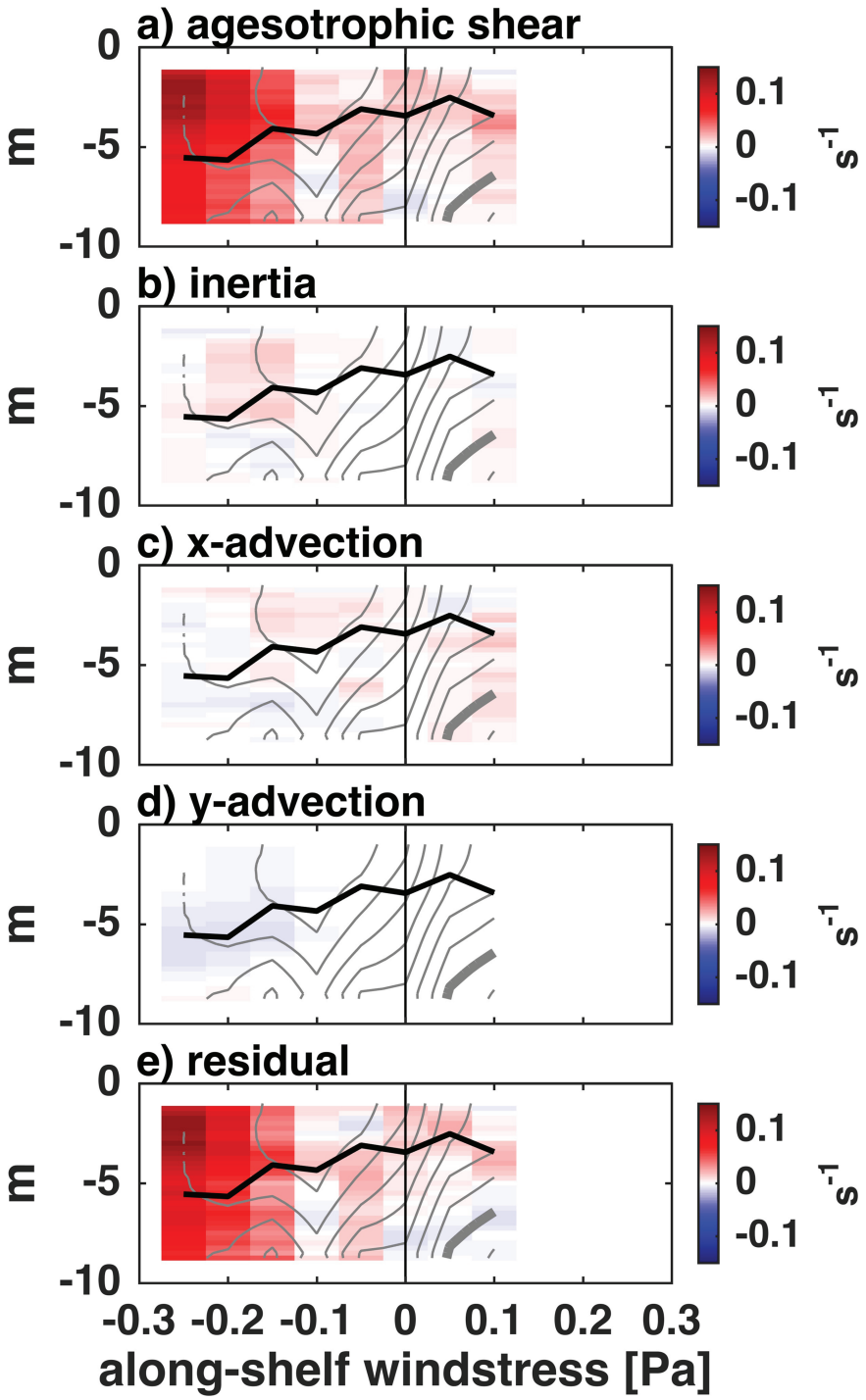

Figure 7. Cross-shelf momentum balance following equation (4) binned as a function of wind stress. (a) Ageostrophic shear (AGEOS); (b) inertia; advection in the (c) cross-shelf and (d) along-shelf directions; and (e) the residual. Density is contoured in intervals of 0.5 σ_t, thick gray line denotes 24 σ_t which is an approximate limit for the CBP, and surface mixed layer depth is plotted in black.

Equation (4) reveals that AGEOS can be generated by vertical changes in local time rate of change of u (inertia), cross-shelf (x-adv), along-shelf (y-adv) and vertical (z-adv) advection of u, and cross-shelf stress divergence (stress div). Combining observations from moorings N2, N3, S2,and S3, all terms in equation (4) can be estimated, with the exception of the last two on the right-hand side (vertical advection and stress divergence). Inertia was estimated by first averaging u between S2 and S3 and then taking vertical and time derivatives using centered differences; x-adv was estimated by multiplying u averaged between S2 and S3 by the cross-shelf gradient of u obtained by centered differences using data from S2 and S3; y-adv was estimated using averaged v multiplied by the along-shelf gradient of u using centered differences, which was done using the mooring pairs N2-S2 and N3-S3, and finally taking the average of the estimates. Its important to note that small scale along-shelf variability will not be resolved between the N and S mooring lines since they are distanced nearly 29 km apart (Figure 1), which could potentially lead to an underestimate of the y-adv term. The remaining two terms (vertical advection and stress divergence) were combined into what will be referred to as the "residual," determined by residual = AGEOS - (inertia + x-adv + y-adv).

Results from the dynamical balance following equation (4) were binned by wind stress classes and are shown in Figure 7. As discussed previously, AGEOS is especially enhanced and plays an important role in the dynamics during strong downwelling-favorable winds (Figure 6). The residual term, is at least an order of magnitude larger than inertial, x-adv and the y-adv terms. In the absence of direct stress measurements, it is not possible to properly separate z-adv from stress div. However, the magnitude of z-adv may be obtained from scaling analysis, and it will be shown that z-adv$\ll$stress div, and is therefore negligible. From observations of cross-shelf velocity (Figure 5) $\partial u/\partial z \approx 0.015\ \mathrm{s}^{-1}$, w is of order 10^{-5} m/s (Lentz, 1995) and assuming it goes from 0 at the surface to maximum value at midwater column (5 m), then $\partial w/\partial z \approx 2\times10^{-6}\ \mathrm{s}^{-1}$, and $f = 8.65\times10^{-5}\ \mathrm{s}^{-1}$. Based on these estimates, z-adv$\approx 3\times10^{-4}\ \mathrm{s}^{-1}$, and therefore 3 orders of magnitude smaller than AGEOS (Figure 7), which points to stress div as the only possible mechanism for generations of AGEOS.

To infer the potential enhancement of turbulence and viscous stresses (stress div), we analyze the gradient Richardson number (R_i), defined as the ratio of the squares of buoyancy frequency (N^2) and shear (S^2):

$$R_i = \frac{N^2}{S^2} = \frac{-\frac{g}{\rho_o}\frac{\partial \rho}{\partial z}}{\left(\frac{\partial u}{\partial z}\right)^2 + \left(\frac{\partial v}{\partial z}\right)^2}. \tag{5}$$

Figure 8 shows the results for N^2, S^2, and a probability density function (PDF) of R_i below the seminal critical value of 0.25 (Miles, 1961), which indicates active mixing due to turbulent overturning. Stratification (N^2) is enhanced during weak winds and below the SML. Note that even during strong downwelling-favorable winds, stratification is nonnegligible in the interior, below 5 m. Shear (S^2) is mostly enhanced in the interior during strong winds. PDF of critical R_i reveal active mixing in the SML during strong winds, and for the most extreme conditions where $\tau_y^w < -0.2$, active mixing was observed in the entire water column, including the interior region. As suggested by Lentz (2001), the downstream along-shelf freshwater transport in the CBP potentially provides a source of buoyancy that is capable of maintaining the stratification, even in the presence of active vertical mixing.

Based on evidences from the vertical gradients of cross-shelf momentum budget (equation (4) and Figure 7), scaling analysis of w-adv, and diagnostic of active mixing based on R_i (Figure 8), we conclude that viscous stresses (stress div) are therefore responsible for the breakdown of thermal wind balance and generation of AGEOS.

4. Discussion

Lentz et al. (1999) have previously compared TWS with OBS at a few locations and depths in our study region. Using time series data obtained from point measurements of currents and density from moored instrumentation distributed between 8 and 26 m isobaths, and depths 4.4–12.7 m below the surface, the authors found that TWS were statistically correlated with OBS. Their analysis however did not evaluate the impact of wind forcing and did not distinguish between conditions when CBP was present or absent, which impedes a direct comparison with our results. Our analysis demonstrates that during periods of weak wind forcing, the magnitude of TWS was within one standard error from OBS, and therefore we conclude that

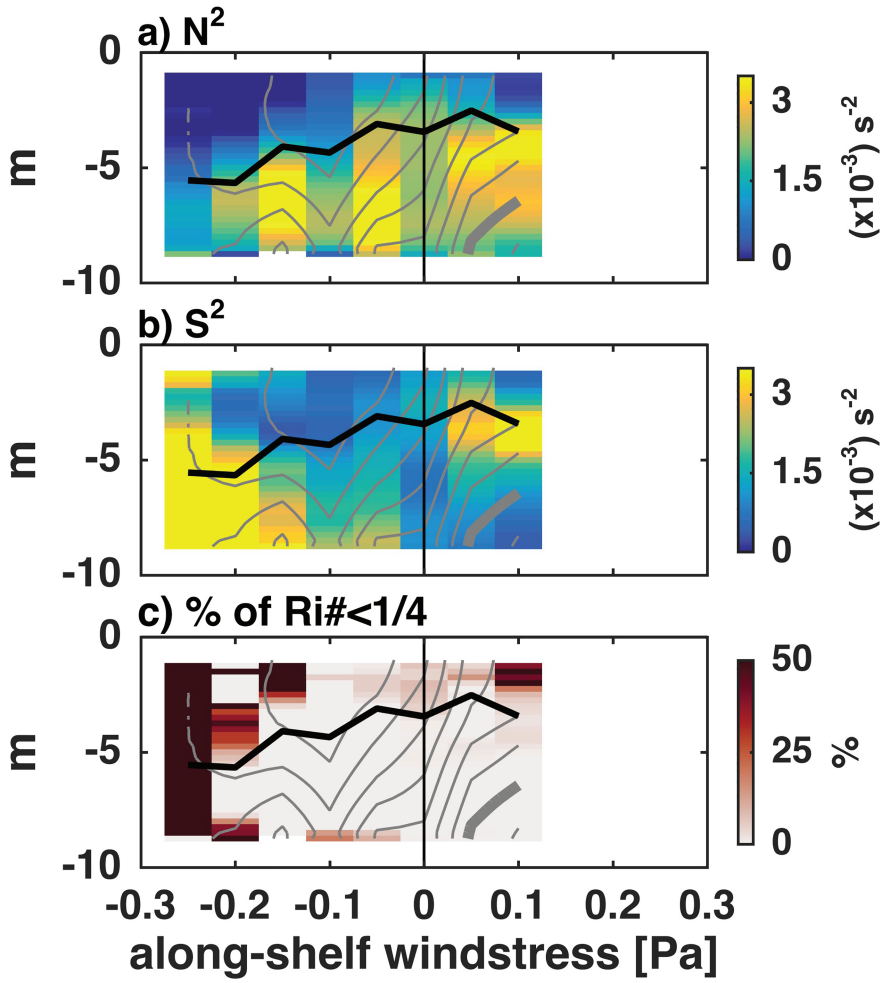

Figure 8. Diagnostic for mixing binned as a function of wind stress: (a) Buoyancy frequency squared (N^2), (b) shear squared (S^2), and (c) percentage of observation of Richardson number below 0.25. Density is contoured in intervals of 0.5 σ_t, thick gray line denotes 24 σ_t which is an approximate limit for the CBP, and mixed layer depth is plotted in black.

the thermal wind balance approximation is valid in the CBP during these conditions (Figure 6). This contradicts previous work from Yankovsky (2006) and Blanton (1981), which indicated that TWS overestimated OBS by approximately a factor or two. It is possible that these discrepancies may arise simply due to contrasting dynamics from different regions and plumes. However, it is important to emphasize that our data set contains a significantly greater number of degrees of freedom given the long time series available, while their conclusions were limited by a smaller number of observations (refer to section 1.1).

In this work we have focused on the role of along-shelf wind forcing, however, as previously noted, downwelling-/upwelling- favorable winds are correlated with onshore/offshore winds. As a consequence, cross-shelf wind stress may generate along-shelf Ekman currents that contribute to AGEOS. To evaluate the role of cross-shelf winds on AGEOS, surface Ekman along-shelf shear ($\partial v_E/\partial z$) can be estimated assuming a linear Ekman velocity profile, and can be calculated as $\partial v_e/\partial z = -2\tau_x/\rho_o f h_e^2$, where h_E is the surface Ekman layer depth. Using the SML for h_E provides an upper bound estimate for addressing the role of surface Ekman along-shelf shear contribution to AGEOS. Focusing on the strongest downwelling wind event, around days 121–122 (Figure 2), with onshore winds peaking at 0.1 Pa and SML reaching 7 m deep, we estimate $\partial v_E/\partial z$ to be 0.05 s^{-1}. This upper bound estimate is less than 27% of the magnitude of AGEOS, and therefore we conclude that along-shelf Ekman shear generated by cross-shelf wind stress is not capable of explaining the AGEOS in the CBP during our observational field campaign.

Yankovsky (2006) hypothesized that breaking of remotely generated internal waves was a potential mechanism for enhanced turbulence generation, and responsible for the disruption of the thermal wind balance.

While our data set can not resolve internal waves there is strong evidence that wind forcing is the major source of energy for turbulence generation leading to enhanced viscous stresses in the CBP. This evidence includes: increase of AGEOS, decrease of stratification, and increase of mixing (R_i <0.25), as winds increased (Figures 7 and 8). In addition, as wind forcing increased, a downward propagation of mixing becomes evident (Figure 8), which again corroborates the hypothesis that winds are the major source of energy for turbulence generation in the CBP.

This downward increase in the reach of turbulence in response to wind forcing, also hinders the possibility of bottom stress being the major driver of turbulence and mixing. A comparison between wind and bottom stresses can be made by estimating bottom stress ($\vec{\tau}_b$) using a quadratic law: $\vec{\tau}_b = \rho_o C_d |\vec{u}_b| \vec{u}_b$, where $C_d = 3 \times 10^{-3}$ is a nondimensional drag coefficient, and $\vec{u}_b$ is the nearest velocity measurement to the bottom (averaged between S2 and S3). The comparison reveals that wind stress magnitude is, on average, over 20 times larger than bottom stress, which in addition to stratification being maintained in the interior, leads us to rule out the importance of bottom stress as a significant source of energy for turbulence generation in the CBP.

A noteworthy result from this work is that AGEOS is predominantly positive, but OBS and TWS switch signs from negative during downwelling, to positive during upwelling (Figures 5e–5g). While TWS magnitudes are not symmetric around zero wind stress, OBS presents a larger asymmetry, with magnitudes that are nearly twice as large during upwelling when compared to downwelling winds of similar strength. This discrepancy leads to OBS magnitudes being smaller than TWS during downwelling, but greater during upwelling, hence AGEOS is positive in both cases. We speculate that differences in stratification between upwelling and downwelling conditions can explain the contrast in OBS. During downwelling, isopycnals tend to be sloped vertically as an advective result of the cross-shelf Ekman driven circulation acting on the density field, decreasing the plume stratification. During upwelling the opposite is observed, with cross-shelf Ekman driven circulation flattening isopycnals, increasing stratification. Therefore, for a given stress, during downwelling, the reduced stratification should lead to an increase in the eddy viscosity and a reduction in the OBS, while during upwelling the increased stratification should lead to a decrease in the eddy viscosity and an enhancement of the OBS.

The potential important effect of waves was not explicitly included in our momentum budget analysis (equation (4)). Lentz et al. (1999) demonstrated that within the inner-shelf of our study region, wave forcing is an order one term in the depth-averaged cross-shelf momentum balance. Observations obtained by the U.S. Army Corps of Engineers using a Waverider Buoy moored at 17.4 m deep in our study region (36°12′N 75°42.9′W), revealed that waves were generally small during our study period, rarely exceeding 1–1.5 m, except during a storm event that took place between Days 120–124. During the storm, significant wave height (H_{sig}) reached 3 m, with dominant wave periods of 10 seconds, propagating from E-NE directions, approaching the shore at an angle of approximately 15°. The contribution of Hasselmann wave stress (τ_x^H) or Stokes-Coriolis forcing (Hasselmann, 1970) to the vertical shear of along-shelf agesotrophic currents can be estimated as

$$\frac{1}{f}\frac{\partial}{\partial z}\left(-\frac{1}{\rho_o}\frac{\partial \tau_x^H}{\partial z}\right) = \frac{\partial v_{st}}{\partial z} = \frac{H_{sig}^2 \omega k^2}{8}\frac{\sinh[2k(z+h)]}{\sinh^2 kh}\sin(\theta_w), \tag{6}$$

where v_{st} is the Stokes drift velocity in the along-shelf direction, ω is the wave frequency, k the wave number, h the water depth and θ_w the wave direction relative to offshore ($\theta_w = 180°$ for waves propagating directly onshore). Using wave properties observed during the storm in equation (6), a maximum shear in the water column is 10^{-3} s^{-1}, 2 orders of magnitude smaller than AGEOS (Figure 5). Lentz et al. (2008) showed that the other wave forcing terms did not contribute significantly to water column shear. The importance of gradients in radiation stress due to wave shoaling are largely balanced by wave stresses, which are limited to the wave boundary layer. Thus, we conclude that wave forcing does not contribute significantly to AGEOS when compared to viscous stresses in the CBP.

4.1. Implications for River Plume Transport

The assumption of geostrophic balance has been widely used in the literature to estimate along-shelf baroclinic transport in river plumes, both from numerical model results (e.g., Fong & Geyer, 2002; Moffat & Lentz, 2012; Pimenta & Kirwan, 2014; Pimenta et al., 2011) and observations (e.g., Chant et al., 2008; Chant

et al., 2008; Geyer et al., 2004; Mazzini et al., 2014). Pimenta et al. (2011) provided a thorough discussion of scalings to estimate plume baroclinic transports under the assumption of geostrophic balance. The plume baroclinic transport (T), can be estimated given the latitude, plume geometry and density anomaly, according to

$$T = \gamma_o \frac{g_p' h^2}{2f}, \tag{7}$$

where γ_o is a parameter dependent on the ratio of the front and the plume cross-shelf widths, $g_p' = g\Delta\rho/\rho_o$ is the plume reduced gravity, g is the gravitational acceleration, $\Delta\rho$ the difference between plume density at the coast and ambient ocean density, ρ_o a reference density, h is the plume maximum thickness (where front intersects the bottom), and f is the Coriolis parameter. According to Pimenta et al. (2011), γ_o is bounded by two limits, from $\gamma_o = 1$ in the case of a narrow, two-layer or Margules front (Margules, 1906), to $\gamma_o = 1/3$ in the case of a constantly stratified and sheared plume.

Results presented here indicate that geostrophic balance holds in the entire water column during weak winds ($|\tau_y^w| < 0.075$ Pa), which supports the validity of equation (7) under these conditions. However, as discussed previously, during strong winds the geostrophic balance breaks down. Our analysis suggests that the predicted transport according to equation (7), could overestimate the observed baroclinic transport by up to 50% during strong downwelling-favorable winds ($\tau_y^w < -0.125$ Pa), and underestimate the observed baroclinic transport by up to 65% during moderate upwelling-favorable winds ($\tau_y^w >0.075$ Pa). This work therefore highlights the importance of including the ageostrophic dynamics in scalings of plume transport under strong wind forcing, and encourages new theoretical development in future studies.

5. Summary and Conclusions

High-resolution time series measurements of currents, vertical and cross-shelf density gradients, which resolved the interior and near-surface (0.5–1 m deep) regions of the water column, were obtained by a combination of Wirewalkers equipped with CTDs, and bottom-mounted and sub-surface ADCPs, moored on the Virginia and North Carolina shelves. This unique 38-day long data set allowed the careful examination of the thermal wind balance in the far-field region of the Chesapeake Bay Plume under a range of wind forcing conditions.

Our observations reveal that during weak wind forcing conditions ($|\tau_y^w| <0.075$ Pa), thermal wind balance is a valid approximation for the first order cross-shelf momentum balance throughout the entire water column in this plume. However, moderate to strong winds can lead to significant deviations from this balance. During strong downwelling-favorable winds ($\tau_y^w <-0.125$ Pa), TWS shear exceeded OBS by a factor of 1.7–2 in the interior, and 3–3.9 in the SML. An opposite response was observed during moderate upwelling-favorable winds ($0.075< \tau_y^w <0.125$ Pa), when OBS was larger than TWS, by a factor of 1.7 in the interior, and 1.3 in the SML. Neither downwelling-favorable winds larger than |0.3| Pa nor upwelling-favorable winds larger than |0.15| Pa were observed during our experiment, and therefore more extreme conditions could not be tested here. While river plume transport scalings have previously assumed geostrophic balance, our work suggests that the ageostrophic component of transport is significant in river plumes under strong wind forcing.

Evidences found in this work, especially the gradual downward propagation of enhanced mixing and decreased stratification as a function of wind forcing, strongly suggests that the main source of energy for turbulence generation is provided by the wind. The enhanced wind generated turbulence increase the relative importance of viscous stresses in the water column, which are responsible for the breakdown of the thermal wind balance, and generation of AGEOS.

Finally, this work emphasizes the importance of obtaining direct in situ measurement of stress in the future, particularly in the near-surface region of the water column, to further advance our understanding of river plume dynamics. Longer time series are also crucial to properly separate the roles of cross- and along-shelf winds, waves, and capturing extreme wind events, both in surface trapped and bottom advected plumes.

Acknowledgments
This study was supported by the National Science Foundation through Grant OCE 1334231. We thank Ken Roma from R/V *Arabella* for his incredible support in our daily cruises to survey CBP. We also thank the Crew and Captains of the R/V *Sharp* and R/V *Savannah* for their efforts in deploying and recovering the moored instrumentation. Eli Hunter was responsible for preprocessing the data and provided invaluable assistance with field work and data collection. The data used in this publication are available in an open access repository (https://doi.org/10.5281/zenodo.3525394) or by contacting the author.

References

Austin, J. A., & Lentz, S. J. (2002). The inner shelf response to wind-driven upwelling and downwelling. *Journal of Physical Oceanography*, *32*(7), 2171–2193. https://doi.org/10.1175/1520-0485(2002)032<2171:TISRTW>2.0.CO;2

Avicola, G., & Huq, P. (2003). The characteristics of the recirculating bulge region in coastal buoyant outflows. *Journal of Marine Research*, *61*(4), 435–463.

Blanton, J. O. (1981). Ocean currents along a nearshore frontal zone on the continental shelf of the southeastern United States. *Journal of Physical Oceanography*, *11*, 1627–1637.

Chant, R. J. (2011). 2.11—Interactions between estuaries and coasts: River plumes their formation, transport, and dispersal. In E. Wolanski, & D. McLusky (Eds.), *Treatise on estuarine and coastal science* pp. 213–235). Waltham: Academic Press. https://doi.org/10.1016/B978-0-12-374711-2.00209-6

Chant, R. J., Glenn, S. M., Hunter, E., Kohut, J., Chen, R. F., Houghton, R. W., et al. (2008). Bulge formation of a buoyant river outflow. *Journal of Geophysical Research*, *113*, C01017. https://doi.org/10.1029/2007JC004100

Chant, R. J., Wilkin, J., Zhang, W., Choi, B.-J., Hunter, E., Castelao, R., et al. (2008). Dispersal of the Hudson River plume in the New York Bight: Synthesis of observational and numerical studies during LaTTE. *Oceanography*, *21*(4), 148–161.

Chapman, D. C., & Lentz, S. J. (1994). Trapping of a coastal density front by the bottom boundary layer. *Journal of Physical Oceanography*, *24*(7), 1464–1479.

Chen, S.-Y., & Chen, S.-N. (2017). Generation of upwelling circulation under downwelling-favorable wind within bottom-attached, buoyant coastal currents. *Journal of Physical Oceanography*, *47*(10), 2499–2519. https://doi.org/10.1175/JPO-D-16-0271.1

Fewings, M., Lentz, S. J., & Fredericks, J. (2008). Observations of cross-shelf flow driven by cross-shelf winds on the inner continental shelf. *Journal of Physical Oceanography*, *38*(11), 2358–2378. https://doi.org/10.1175/2008JPO3990.1

Fong, D. A., & Geyer, W. R. (2001). The response of a river plume during an upwelling favorable wind event. *Journal of Geophysical Research*, *106*, 1067–1084.

Fong, D. A., & Geyer, W. R. (2002). The alongshore transport of freshwater in a surface-trapped river plume. *Journal of Physical Oceanography*, *32*, 957–972.

Garvine, R. W. (1995). A dynamical system for classifying buoyant coastal discharges. *Continental Shelf Research*, *15*, 1585–1596.

Garvine, R. W. (2004). The vertical structure and subtidal dynamics of the inner shelf off New Jersey. *Journal of Marine Research*, *62*(3), 337–371.

Geyer, W. R., Hill, P. S., & Kineke, G. C. (2004). The transport, transformation and dispersal of sediment by buoyant coastal flows. *Continental Shelf Research*, *24*(7), 927–949. https://doi.org/10.1016/j.csr.2004.02.006

Geyer, W. R., Signell, R. P., Fong, D. A., Wang, J., Anderson, D. M., & Keafer, B. P. (2004). The freshwater transport and dynamics of the western Maine coastal current. *Continental Shelf Research*, *24*, 1339–1357.

Halliwell, G. R. Jr., George, R., & Allen, J. S. (1987). The large-scale coastal wind field along the west coast of North America, 19811982. *Journal of Geophysical Research*, *92*(C2), 1861–1884. https://doi.org/10.1029/JC092iC02p01861

Hasselmann, K. (1970). Wave driven inertial oscillations. *Geophysical Fluid Dynamics*, *1*(3-4), 463–502. https://doi.org/10.1080/03091927009365783

Hetland, R. D. (2017). Suppression of baroclinic instabilities in buoyancy-driven flow over sloping bathymetry. *Journal of Physical Oceanography*, *47*(1), 49–68. https://doi.org/10.1175/JPO-D-15-0240.1

Hickey, B. M., Kudela, R. M., Nash, J. D., Bruland, K. W., Peterson, W. T., MacCready, P., et al. (2010). River influences on shelf ecosystems: Introduction and synthesis. *Journal of Geophysical Research*, *115*, C00B17. https://doi.org/10.1029/2009JC005452

Hill, A. E. (1998). Buoyancy effects in coastal and shelf seas. In A. R. Robinson, & K. H. Brink (Eds.), *The sea* (Vol. 11, pp. 63–88). Hoboken, New Jersey: John Wiley & Sons, Inc.

Horner-Devine, A. R., Hetland, R. D., & MacDonald, D. G. (2015). Mixing and transport in coastal river plumes. *Annual Review of Fluid Mechanics*, *47*(1), 569–594. https://doi.org/10.1146/annurev-fluid-010313-141408

Jia, Y., & Yankovsky, A. E. (2012). The impact of ambient stratification on freshwater transport in a river plume. *Journal of Marine Research*, *70*, 69–92.

Jurisa, J. T., & Chant, R. J. (2013). Impact of offshore winds on a buoyant river plume system. *Journal of Physical Oceanography*, *43*, 2571–2587.

Large, W. G., & Pond, S. (1981). Open ocean momentum flux measurements in moderate to strong winds. *Journal of Physical Oceanography*, *11*, 324–336.

Lentz, S. J. (1995). Sensitivity of the inner-shelf circulation to the form of the eddy viscosity profile. *Journal of Physical Oceanography*, *25*(1), 19–28. https://doi.org/10.1175/1520-0485(1995)025<0019:SOTISC>2.0.CO;2

Lentz, S. J. (2001). The influence of stratification on the wind-driven cross-shelf circulation over the North Carolina shelf. *Journal of Physical Oceanography*, *31*(9), 2749–2760. https://doi.org/10.1175/1520-0485(2001)031<2749:TIOSOT>2.0.CO;2

Lentz, S. J. (2004). The response of buoyant coastal plumes to upwelling-favorable winds. *Journal of Physical Oceanography*, *34*(11), 2458–2469.

Lentz, S. J., Fewings, M., Howd, P., Fredericks, J., & Hathaway, K. (2008). Observations and a model of undertow over the inner continental shelf. *Journal of Physical Oceanography*, *38*(11), 2341–2357. https://doi.org/10.1175/2008JPO3986.1

Lentz, S. J., Guza, R. T., Elgar, S., Feddersen, F., & Herbers, T. H. C. (1999). Momentum balances on the North Carolina inner shelf. *Journal of Geophysical Research*, *104*(C8), 18,205–18,226. https://doi.org/10.1029/1999JC900101

Lentz, S. J., & Helfrich, K. R. (2002). Buoyant gravity currents along a sloping bottom in a rotating fluid. *Journal of Fluid Mechanics*, *464*, 251–278.

Lentz, S. J., & Largier, J. (2006). The influence of wind forcing on the Chesapeake Bay buoyant coastal current. *Journal of Physical Oceanography*, *36*(7), 1305–1316.

Margules, M. (1906). Über Temperaturschichtung in stationär bewegter und in ruhender Luft. *Meteorologische Zeitschrift*, *23*, 243–254.

Mazzini, P. L. F., Barth, J. A., Shearman, R. K., & Erofeev, A. (2014). Buoyancy-driven coastal currents off Oregon during fall and winter. *Journal of Physical Oceanography*, *44*, 2854–2876. https://doi.org/10.1175/JPO-D-14-0012.1

Mazzini, P. L. F., & Chant, R. J. (2016). Two-dimensional circulation and mixing in the far field of a surface-advected river plume. *Journal of Geophysical Research: Oceans*, *121*, 3757–3776. https://doi.org/10.1002/2015JC011059

Miles, J. (1961). On the stability of heterogeneous shear flows. *Journal of Fluid Mechanics*, *10*, 496–508.

Moffat, C., & Lentz, S. J. (2012). On the response of a buoyant plume to downwelling-favorable wind stress. *Journal of Physical Oceanography*, *42*, 1083–1098.

O'Donnell, J. (2010). The dynamics of estuary plumes and fronts. In A. Valle-Levinson (Ed.), *Contemporary issues in estuarine physics* (pp. 186–246). Cambridge: Cambridge University Press.

Pimenta, F. M., & Kirwan, A. D. Jr. (2014). The response of large outflows to wind forcing. *Continental Shelf Research*, *89*, 24–37. https://doi.org/10.1016/j.csr.2013.11.006

Pimenta, F. M., Kirwan, A. D. Jr., & Huq, P. (2011). On the transport of buoyant coastal plumes. *Journal of Physical Oceanography*, *41*, 620–640.

Pinkel, R., Goldin, M. A., Smith, J. A., Sun, O. M., Aja, A. A., Bui, M. N., & Hughen, T. (2011). The wirewalker: A vertically profiling instrument carrier powered by ocean waves. *Journal of Atmospheric and Oceanic Technology*, *28*(3), 426–435. https://doi.org/10.1175/2010JTECHO805.1

Rainville, L., & Pinkel, R. (2001). Wirewalker: An autonomous wave-powered vertical profiler. *Journal of Atmospheric and Oceanic Technology*, *18*(6), 1048–1051. https://doi.org/10.1175/1520-0426(2001)018<1048:WAAWPV>2.0.CO;2

Sharples, J., Middelburg, J. J., Fennel, K., & Jickells, T. D. (2017). What proportion of riverine nutrients reaches the open ocean? *Global Biogeochemical Cycles*, *31*, 39–58. https://doi.org/10.1002/2016GB005483

Ullman, D. S., Codiga, D. L., Hebert, D., Decker, L. B., & Kincaid, C. R. (2012). Structure and dynamics of the midshelf front in the New York Bight. *Journal of Geophysical Research*, *117*, C01012. https://doi.org/10.1029/2011JC007553

Yankovsky, A. E. (2006). On the validity of thermal wind balance in alongshelf currents off the New Jersey coast. *Continental Shelf Research*, *26*, 1171–1183.

Yankovsky, A. E., & Chapman, D. C. (1997). A simple theory for the fate of buoyant coastal discharges. *Journal of Physical Oceanography*, *27*(7), 1386–1401.